Text Supplement for ScholarWorks@UA collection

Moment tensor catalog results for nuclear explosions, volcanic events, and earthquakes

Celso Alvizuri

Version 1: December 1, 2017
Version 2: May 9, 2018

Attribution: If you use these files, please cite *Alvizuri et al.* (2018) and *Alvizuri* (2017).

Description of files

This collection is established for the submission of a manuscript (*Alvizuri et al.*, 2018).

Three catalogs of seismic moment tensors were generated using first-motion polarities, body waves, and surface waves. The best solution (M_0) was obtained through a grid-search in the moment tensor space using the 'cut-and-paste' (CAP) approach, which allows for different frequencies and time shifts on different portions of seismograms (*Zhao and Helmberger*, 1994; *Zhu and Helmberger*, 1996; *Zhu and Ben-Zion*, 2013). The moment tensor approach was adapted and applied in *Silwal and Tape* (2016) for double couple moment tensors and in *Alvizuri and Tape* (2016) for full moment tensors. **Summary of figures and files in the collection:**

figure	description	file name (# pages)
Figure A1	Waveform fits for 32 events from the Nevada Test Site (NTS) (*Ford et al.*, 2009)	fmtu_llnl_nucs_fits.pdf (17) fmtu_llnl_quakes_fits.pdf (12) fmtu_llnl_coll_fits.pdf (3)
Figure A2	Waveform fits for 63 events from Uturuncu volcano (*Alvizuri and Tape*, 2016)	fmtu_uturuncu_fits.pdf (63)
Figure A3	Waveform fits for 21 events from southern Alaska (*Silwal and Tape*, 2016)	fmtu_alaska_fits.pdf (21)
Figure B1	Uncertainty plots for NTS events	fmtu_llnl_nucs.pdf (17) fmtu_llnl_quakes.pdf (12) fmtu_llnl_coll.pdf (3)
Figure B2	Uncertainty plots for Uturuncu events	fmtu_uturuncu.pdf (63)
Figure B3	Uncertainty plots for Alaska events	fmtu_alaska.pdf (21)
Figure C1	Rayleigh wave time shift maps for nuclear explosions	tshifts_spider_rayl.pdf (17)
Figure D1	Love wave time shift maps for nuclear explosions	tshifts_spider_love.pdf (17)
Figure E1	Time shift plots: one plot per station for NTS events	tshifts_scatter.pdf (25)
	this file	`Alvizuri2017catalog_v2.pdf`
	description of data availability, data access, data processing, and details related to *Walter et al.* (2006)	`Alvizuri2017catalog_data.pdf`

Within the sets of figures, the 32 NTS events are in the same order as in *Ford et al.* (2009, Table 1), and the Uturuncu events and Alaska events are ordered by origin time.

Figures A1, A2, A3: Waveform fits

Waveform fits for 63 moment tensor inversions for which waveform misfit is plotted on the source-type plot. (Figure B). Black are observed waveforms; red are synthetic waveforms computed using a frequency-wavenumber method (*Zhu and Rivera*, 2002) that assumes a (1D) layered model. The waveforms are fit separately within five time windows: P wave vertical component (PV), P wave radial component (PR), Rayleigh wave vertical component (SurfV), Rayleigh wave horizontal component (SurfR), and Love wave transverse component (SurfT). At far left in each row is the station name, source-station distance in km, and station azimuth in degrees. Below each pair of waveforms are four numbers: the cross-correlation time shift between data and synthetics, the cross-correlation value, the percent of the misfit function represented by the waveform pair, and the amplitude ratio between waveforms, $\ln(A_{\rm obs}/A_{\rm syn})$, where A is the max value of the waveform within the time window.

The beachball represents the best solution M_0 (i.e., the global minimum of the misfit function). The beachball is plotted as a lower-hemisphere projection (standard seismological convention) of the moment tensor. The surrounding black dots denote the azimuthal location of the stations used, and the red crosses denote the lower hemisphere piercing points of the ray paths to the stations.

Here is a header for an example event in Figure A1:

```
Event HOYA Model wes Depth 1
FM 303 31 65 Mw 4.69 γ -5 δ 66 rms 4.092e-01 VR 83.3 pol_wt 999.00
Filter periods (seconds): Body:0.17-1.43. Surf:6.67-33.33 duration: 0.10/0.05 s
# norm L1  # Pwin 3 Swin 300  # N 19 Np 0 Ns 55
```

The four header lines are as follows:

1. `Event HOYA Model wes Depth 1`
   The event name is from Table 2 of *Alvizuri et al.* (2018). The layered model used is `wes`, and the event depth is 1 km.

2. `FM 303 31 65 Mw 4.69 γ -5 δ 66 rms 4.092e-01 VR 83.3 pol_wt 999.00`
   The orientation of the moment tensor solution M_0 is strike 303°, dip 31°, rake 65°. The estimated magnitude is $M_{\rm w}$ 4.69. The source type of M_0 is expressed in terms of lune longitude $\gamma = -5°$ and lune latitude $\delta = 66°$. The waveform difference between data and synthetics is $RMS = 0.4092$, and the variance reduction is $VR = 83.3\%$. These are based on a waveform difference measure that rewards using longer time windows and broader bandpass limits. This choice means that the VR cannot be directly compared with VR values reported in other studies.

   If polarities are use in the misfit function, then the factor `pol_wt` determines the balance between fitting waveforms and fitting polarities. A value of 999.0 means that polarities are not used.

3. `Filter periods (seconds): Body:0.17-1.43. Surf:6.67-33.33 duration: 0.10/0.05 s`
   The body waves were filtered 0.17–1.43 s, the surface waves were filtered 6.67–33.33 s.
   The source time function is a trapezoidal function whose duration is 0.10 s and whose rise time is half the duration. The duration is not an estimated source parameter but is set according to the target frequency of body waveforms (here 0.7–6 Hz).

4. `# norm L1  # Pwin 3 Swin 300  # N 19 Np 0 Ns 55`
   An L1 norm was used for the misfit function (e.g., *Silwal and Tape*, 2016). The (reference) P-window is 3 s long and the surface wave window is 300 s long. There are 21 stations (N), 0 P wave windows (Np), and 55 surface wave windows (Ns).[1]

The numbers below each station are

1. source–station epicentral distance, km
2. station azimuth, in degrees
3. time shift between picked P onset and synthetic P onset.
4. sign of the observed first-motion polarity[2], which is either 1 (up or compression) or -1 (down or dilatation). The number in parentheses is the predicted amplitude, which ranges between $\pm\sqrt{2}$; numbers close to zero indicate that the station is near a nodal surface of the radiation pattern for the assumed mechanism.

The four numbers below each pair of waveforms are

1. the cross-correlation time shift $\Delta T = T_{\text{obs}} - T_{\text{syn}}$ required for matching the synthetics $s(t)$ with the data $u(t)$. A positive time-shift means that the synthetics arrive earlier than the data and that the assumed velocity model is faster than the actual earth structure.
2. the maximum cross-correlation percentage between $u(t)$ and $s(t - \Delta T)$
3. the percentage of the total misfit
4. the amplitude ratio $\ln(A_{\text{obs}}/A_{\text{syn}})$ in each time window

Figures B1, B2, B3: Uncertainty plots

Alvizuri et al. (2018), Figure 5, caption:
Full moment tensor uncertainty summary for the HOYA nuclear explosion.
(a) Map of source location (red star) and stations used in the inversion for this event. (b) Contour plot of the polarity misfit on the lune, if polarities had been used, as for the Uturuncu events (*Alvizuri and Tape*, 2016). (c) Source type probability density $p(v, w)$ in the vw rectangle (*Tape and Tape*, 2015). A green circle indicates the location of the point (v_x, w_x) where p is maximum; this point is apt to differ from the source type (v_0, w_0) of M_0. (d) Contour plot of the variance reduction $VR(\mathbf{\Lambda})$. At each point $\mathbf{\Lambda}$, the variance reduction $VR(\mathbf{\Lambda})$ is the maximum variance reduction $VR(M)$ for moment tensors M that have source type $\mathbf{\Lambda}$. Large values (blue) of VR represent better fit between observed and synthetic waveforms. Of the beachballs $M(\mathbf{\Lambda})$, our solution M_0 (green box) is the one with largest VR. The gray arcs on the lune are the great circle arcs $\lambda_1 = 0$, $\lambda_2 = 0$, and $\lambda_3 = 0$; they as well as other lune details are the same as in Figure 2, left. Selected eigenvalue triples (black dots) on the boundary of the lune are indicated,

[1] For the case of the NTS events, the will generally be a discrepancy between the N in the header and the number of stations listed in Figure 3, which shows the unique number of stations used. Stations that are multiply listed for networks (e.g., TS.PFO and CI.PFO) or stations with different sensors for high-frequency and broadband recordings (e.g., LL.MNV.BB and LL.MNV.HF) would only get counted once in Figure 3 but multiple times for the N header.

[2] First-motion polarity measurements were only used for the events at Uturuncu volcano (*Alvizuri and Tape*, 2016).

with the understanding that the triples need to be normalized. The positive isotropic source $(1, 1, 1)$ is at the top, the negative isotropic source $(-1, -1, -1)$ is at the bottom, and the double couple $(1, 0, -1)$, not shown, would be at the center of the lune. (e) The curves $\hat{V}'(\omega)$ and $\hat{P}'(\omega)$ that are used to construct the confidence curve $\mathscr{P}(V)$ in (f), as explained in *Silwal and Tape* (2016) in the context of double couples. For full moment tensors, as here, $\hat{V}'(\omega) \propto \sin^4 \omega$. (f) The confidence curve $\mathscr{P}(V)$ for M_0. The more the curve resembles the shape of a capital gamma (Γ), the better. The shaded area is the average confidence $\mathscr{P}_{\text{AV}}$. (g) The moment tensor M_0, plotted in a lower-hemisphere projection. The location of the piercing point for each station depends on the station azimuth, epicentral distance, and the assumed layered reference model.

Figure C1: Time shift maps per event

For each event shown in Figure A1, we can collect the time shifts for Rayleigh waves and Love waves and plot them as "spider" plots. These plots are useful in assessing the possibility of cycle skipping between observed and synthetic waveforms. Since the time shifts are expected to be caused by differences between real Earth structure and the assumed 1D Earth structure, we expect the time shift patterns to be smoothly varying as the station azimuth changes. However, the time shifts can also be caused by errors in the assumed source hypocenter or origin time; hence we also examine the time shift plots per station (Figure D1).

Figure D1: Time shift plots per station

For all the time shifts for Rayleigh waves and Love waves shown in Figure A1, we collect them by station to make the plots in Figure D1. These plots have the advantage over the time shift maps in Figure C1 in that the systematic influence of source errors will be reduced in Figure D1 (all sources, one station) vs Figure C1 (one source, all stations).

Note that different bandpasses were used for different events (Table 3); an alternative to showing the time shift would be to divide by the center of the bandpass and then plot the phase shift.

Text file tables for moment tensor catalogs [`fmtu_XXXX_mech_extended.txt`]

Seismic moment tensor catalogs. Details can be found within the header lines, which also refer to *Kanamori* (1977); *Aki and Richards* (1980); *Silver and Jordan* (1982); *Minson et al.* (2007); *Tape and Tape* (2012, 2013, 2015).

Input text files used in the moment tensor inversion [`fmtu_weights_XXXX.zip`]

We provide a text file for each of the 63 events in this study. These files show which stations and which time windows were used (or not) in each moment tensor inversion. It also shows the first-motion polarity observations that were used.

References

Aki, K., and P. G. Richards (1980), *Quantitative Seismology, Theory and Methods*, W. H. Freeman, San Francisco, Calif., USA.

Alvizuri, C. (2017), Moment tensor catalog results for nuclear explosions, volcanic events, and earthquakes, ScholarWorks@UA at `http://hdl.handle.net/11122/8007` (last accessed 2018-05-09): descriptor file, text files of catalogs, and composite figures of waveform fits, uncertainty results, and time shifts.

Alvizuri, C., and C. Tape (2016), Full moment tensors for small events ($M_w < 3$) at Uturuncu volcano, Bolivia, *Geophys. J. Int.*, *206*, 1761–1783, doi:10.1093/gji/ggw247.

Alvizuri, C., V. Silwal, L. Krischer, and C. Tape (2018), Estimation of full moment tensors, including uncertainties, for nuclear explosions, volcanic events, and earthquakes, *J. Geophys. Res. Solid Earth* (in press), doi:10.1029/2017JB015325.

Ford, S. R., D. S. Dreger, and W. R. Walter (2009), Identifying isotropic events using a regional moment tensor inversion, *J. Geophys. Res.*, *114*, B01306, doi:10.1029/2008JB005743.

Kanamori, H. (1977), The energy release in great earthquakes, *J. Geophys. Res.*, *82*, 2981–2987.

Minson, S. E., D. S. Dreger, R. Bürgmann, H. Kanamori, and K. M. Larson (2007), Seismically and geodetically determined nondouble-couple source mechanisms from the 2000 Miyakejima volcanic earthquake swarm, *J. Geophys. Res.*, *112*, B10308, doi:10.1029/2006JB004847.

Silver, P. G., and T. H. Jordan (1982), Optimal estimation of scalar seismic moment, *Geophys. J. R. Astron. Soc.*, *70*, 755–787.

Silwal, V., and C. Tape (2016), Seismic moment tensors and estimated uncertainties in southern Alaska, *J. Geophys. Res. Solid Earth*, *121*, 2772–2797, doi:10.1002/2015JB012588.

Tape, W., and C. Tape (2012), A geometric setting for moment tensors, *Geophys. J. Int.*, *190*, 476–498, doi:10.1111/j.1365-246X.2012.05491.x.

Tape, W., and C. Tape (2013), The classical model for moment tensors, *Geophys. J. Int.*, *195*, 1701–1720, doi:10.1093/gji/ggt302.

Tape, W., and C. Tape (2015), A uniform parameterization of moment tensors, *Geophys. J. Int.*, *202*, 2074–2081, doi:10.1093/gji/ggv262.

Walter, W. R., K. D. Smith, J. L. O'Boyle, T. F. Hauk, F. Ryall, S. D. Ruppert, S. C. Myers, R. Abbot, and D. A. Dodge (2006), An assembled western United States dataset for regional seismic analysis, ISSO 9660 CD, LLNL release UCRL-MI-222502, available via download request at `https://ds.iris.edu/mda/18-001`.

Zhao, L.-S., and D. V. Helmberger (1994), Source estimation from broadband regional seismograms, *Bull. Seismol. Soc. Am.*, *84*(1), 91–104.

Zhu, L., and Y. Ben-Zion (2013), Parameterization of general seismic potency and moment tensors for source inversion of seismic waveform data, *Geophys. J. Int.*, *194*, 839–843, doi:10.1093/gji/ggt137.

Zhu, L., and D. Helmberger (1996), Advancement in source estimation techniques using broadband regional seismograms, *Bull. Seismol. Soc. Am.*, *86*(5), 1634–1641.

Zhu, L., and L. A. Rivera (2002), A note on the dynamic and static displacements from a point source in multilayered media, *Geophys. J. Int.*, *148*, 619–627, doi:10.1046/j.1365-246X.2002.01610.x.

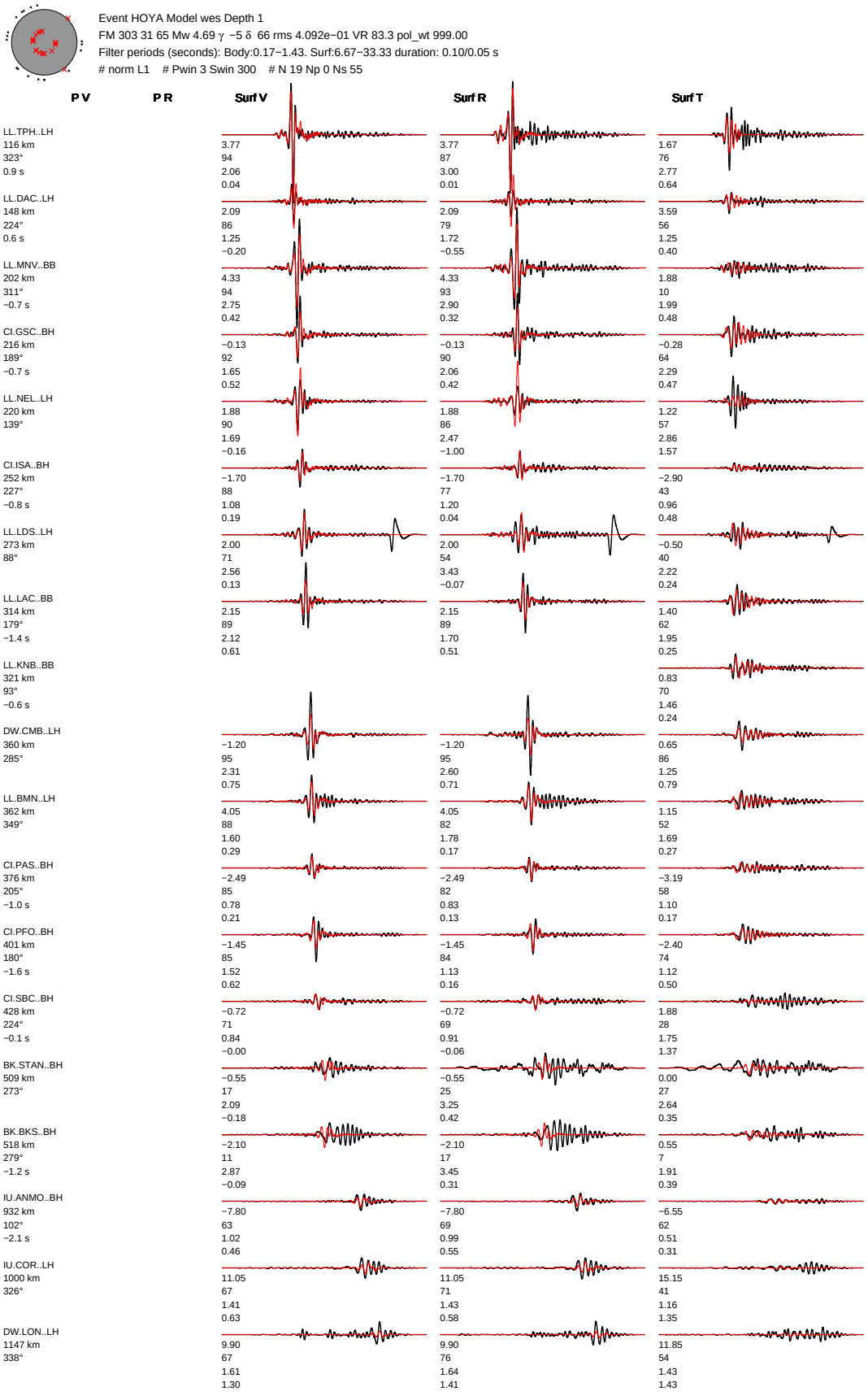

Figure A1-12: Example from p. 12 of the set of 32 events in Figure A1. A slightly modified version of this figure is displayed as Figure 4 in *Alvizuri et al.* (2018). The original version here includes more text labels and also the Love wave fits for LL.KNB.

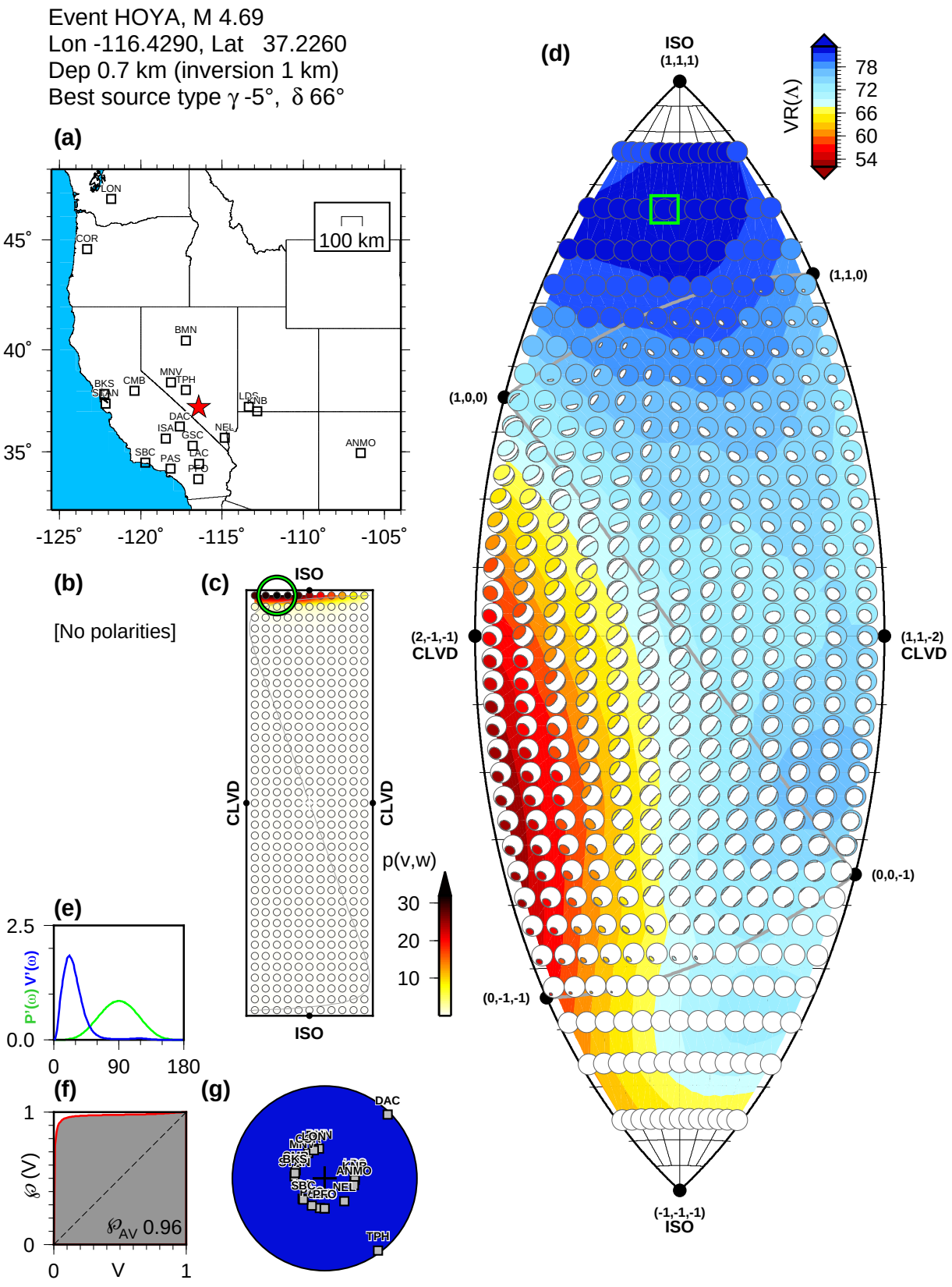

Figure B1-12: Example from p. 12 of the set of 32 in Figure B1. This is displayed as Figure 5 in *Alvizuri et al.* (2018).

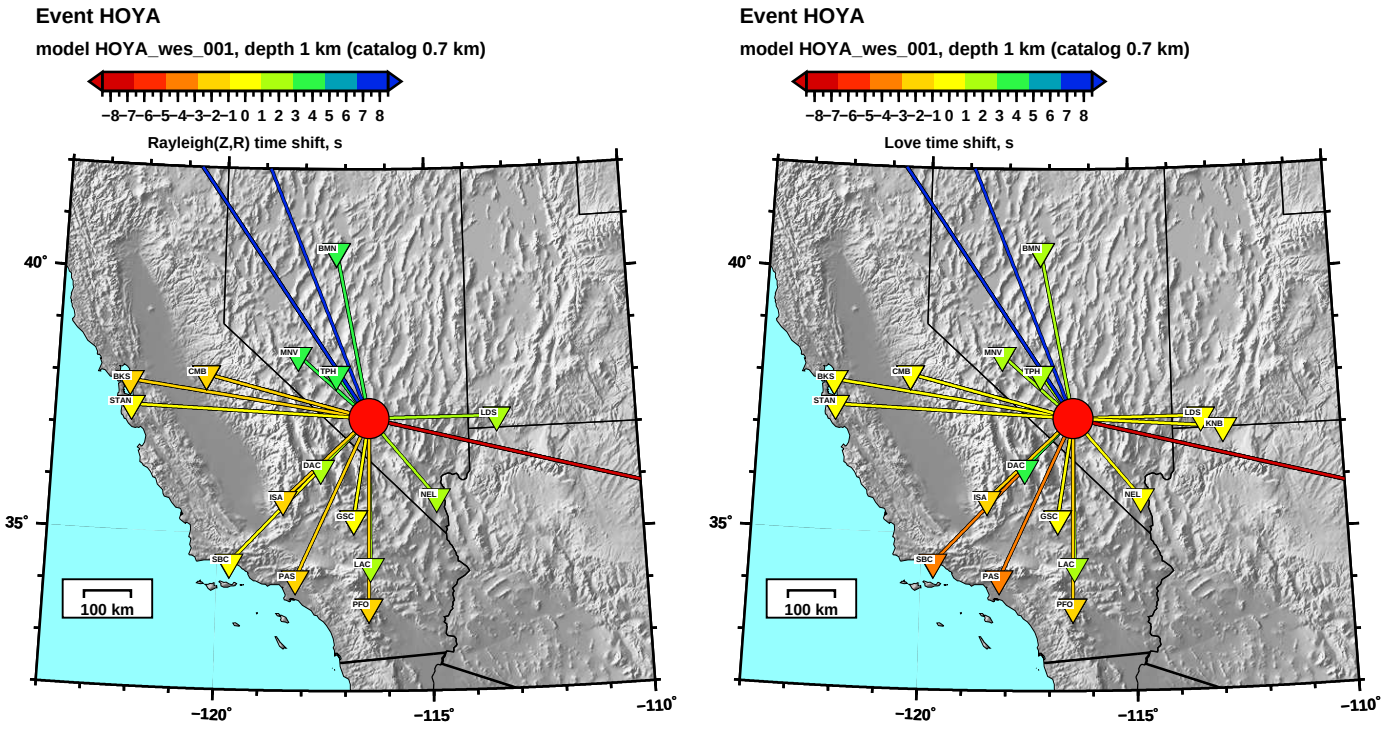

Figure C1-12 and D1-12: (left) Example from p. 12 of the set of 17 in Figure C1. (right) Example from p. 12 of the set of 17 in Figure D1. This is displayed as Figure 6 in *Alvizuri et al.* (2018).